LOI12-15-005

Letter of Intent to PAC 43

Measurement of Double Deeply Virtual Compton Scattering in the di-muon channel with the SoLID spectrometer

Alexandre Camsonne*, Mark K. Jones, Jian-Ping Chen

Thomas Jefferson National Accelerator Facility
12000 Jefferson Avenue, Newport News, Virginia 23606, USA

Marie Boer*, Gabriel Charles, Michel Guidal, Dominique Marchand, Carlos Muñoz Camacho, Silvia Niccolai, Eric Voutier*†

Institut de Physique Nucléaire
IN2P3/CNRS, Université Paris Sud
15 rue Georges Clémenceau, 91406 Orsay, France

Zhiwen Zhao*

Old Dominion University, Department of Physics,
4600 Elkhorn Avenue, Norfolk, VA 23529, USA

Kondo Gnanvo*, Nilanga Linayage, Chao Gu

University of Virginia, Department of Physics,
382 McCormick Rd., PO Box 400714, Charlottesville, VA 22904, USA

Zhihong Ye

Duke University, Department of Physics,
Science Dr., PO Box 90305, Durham, NC 27708, USA

Evaristo Cisbani

Istituto Superiore di Sanità
299 Viale Regina Elena, Roma 00161, Italia

Guido Maria Urcioli

INFN, Sezione di Roma1
2 Piazzale Aldo Moro, Roma 00185, Italia

Vincenzo Bellini, Concetta Maria Sutera

Dipartimento di Fisica a Astronomica, Università di Catania,
64 Via S. Sofia, Catania 95123, Italia

Hamza Atac, Adam Blomberg, Sylvester Joosten, Zein-Eddine Meziani, Michael Paolone, Nikos Sparveris

Temple University, Department of Physics,
Barton Hall A323, 1900 N. 13th Street, Philadelphia, PA 19122, USA

Anthony W. Thomas

ARC Special Research Centre for the Subatomic Structure of Matter (CSSM)
School of Chemistry and Physics, University of Adelaide, Adelaide SA 5005 AUSTRALIA

Hervé Moutarde, Franck Sabatié, Maxime Defurne

DSM/IRFU/SPhN, CEA - Saclay
Bât. 141, Gif sur Yvette 91191, France

Malek Mazouz

Faculté des Sciences de Monastir, Département de physique, 5000-Monastir, Tunisia
Monastir, Tunisia

Paul Gueye

Department of Physics Hampton University
Olin Engineering Building, 268 Emancipation Drive Hampton VA 23668

May 18, 2015

† Contact person
* Spokesperson

Abstract

The Compton scattering of a virtual photon in the deep inelastic regime, or so-called double deeply virtual Compton scattering (DDVCS), constitutes a unique access to generalized parton distributions (GPDs). The virtuality of the final photon allows to investigate in a decorrelated way the x- and ξ-dependences of the GPDs, as opposed to deeply virtual Compton scattering accessing unambiguously GPDs along the diagonals $x = \pm\xi$. This unique feature of DDVCS allows investigation of the ξ-dependence of GPDs which is of relevance, among others, for the determination of the transverse parton densities and the distribution of nuclear forces. This letter proposes to investigate the DDVCS process $ep \to ep\gamma^*$ at 11 GeV incident beam energy in the di-muon channel ($ep\gamma^* \to ep\mu^+\mu^-$) with the SoLID spectrometer supplemented with muon detectors. The experiment would develop according to a parasitic step followed by a dedicated running period. The parasitic run would be parallel to the SoLID J/Ψ experiment and would deliver a significant set of exprimental data about di-muon production at different deep inelastic regimes, and would bring data for GPD physics at $Q^2 > Q'^2$ in a limited phase space region. The dedicated run would involve a strong luminosity increase together with a specific detector configuration to take advantage of the full potential of DDVCS for GPDs phenomenology at 11 GeV.

1 Introduction

The description of the partonic structure of hadronic matter via the Generalized Parton Distributions (GPDs) [1] profoundly renewed and extended the understanding of the structure and dynamics of the nucleon [2, 3]. Providing the link between electromagnetic form factors and parton distributions [4, 5] GPDs unify within the same formalism two different experimental expressions of the same physics reality which is the nucleon structure. Encoding the correlations between partons, GPDs access the internal dynamics of the nucleon as expressed by the Ji sum rule linking GPDs to the angular momentum [6], and the second moment of GPDs giving insights about the distribution of nuclear forces [7]. Consequently, GPDs appear as fundamental building elements of the nuclear structure knowledge, asking for a precise and complete experimental determination.

GPDs can be accessed in the hard scattering regime of exclusive lepto-production processes [4, 5], that is for high-enough quadrimomentum transfer Q^2 of the probe and small-enough quadrimomentum transfer t to the nucleon to allow the probe to couple to partons and ensure the factorization of the reaction amplitude. In addition to these variables, GPDs are also depending on the longitudinal momentum fraction x of the initial parton and on the transferred longitudinal momentum fraction ξ to the final parton. In accordance, GPDs may be interpreted as a $1/Q$ resolution distribution in the transverse plane of partons carrying some longitudinal momentum fraction [8, 9, 10, 11].

The golden reaction channel for GPD mapping in this multi-dimensional space is the deeply virtual Compton scattering (DVCS) where the virtual photon generated by the lepton beam transformed into a real photon after interacting with a parton from the nucleon [12]. GPDs are entering the cross section for this process in terms of Compton form factors which imaginary part involved GPDs at the $x = \pm\xi$ phase-space point while the real part is the convolution integral of GPDs and parton propagators over the whole physics range. In fine, DVCS allows to investigate unambiguously GPDs along the diagonals $x = \pm\xi$ and is therefore limited to a restricted region of the available phase space.

The strict Compton scattering of a virtual photon, in which the final photon remains virtual, has been suggested as a new reaction channel to overcome this limitation [13, 14]. The virtuality of the final state photon in the so-called double deeply virtual Compton scattering (DDVCS) process indeed allows to decouple the experimental x- and ξ-dependences opening off-diagonal investigation of GPDs. However, the combination of cross section smallness and difficult theoretical interpretation of electron induced DDVCS when detecting the e^+e^--pair from the decay of the final virtual photon did forbid up to now any reliable experimental study. Taking advantage of the energy upgrade of the CEBAF accelerator and of the development of SoLID detection capabilities, this letter proposed to investigate the electroproduction of $\mu^+\mu^-$ di-muon pairs and measure the beam spin asymmetry of the exclusive $\vec{e}p \to ep\gamma^* \to ep\mu^+\mu^-$ reaction in the hard scattering regime.

The next section reviews the main characteristics of the DDVCS process and the GPD content of the beam spin asymmetry experimental observable. The benefits of DDVCS measurements for the achievement of the GPD experimental program are specifically discussed in the following section, before adressing the description of the experimental setup constituting of the base SoLID spectrometer and the forseen extension required for the di-muon detection. Finally, the expected counting rates and experimental data are presented based on the simulation package of the SoLID spectrometer and the VGG modeling [15] of the Bethe-Heitler and DDVCS cross sections.

2 Double deeply virtual Compton scattering

2.1 Electroproduction of photons

Similarly than the light diffusion from a material is telling about its internal structure, the light scattered by the nucleon carries information about the parton dynamics and organisation, providing that the wavelength associated to this light is smaller than the nucleon size. The Compton scattering of a virtual photon with quadri-momentum $Q^2 > 1$ (GeV/c^2)^2 is capable of resolving the internal structure of the nucleon. The deep regime of this process, also known as double deeply virtual Compton scattering, is the simplest expression of the hanbag diagram (Fig. 1) allowing to access GPDs.

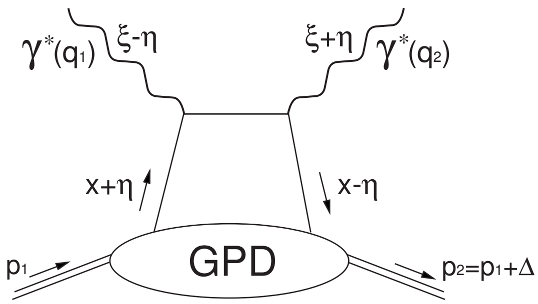

Figure 1: The handbag diagram, symbolizing also the DDVCS process: the initial and final virtual photon momenta are respectively q_1 and q_2, and similarly the initial and final proton momenta are p_1 and p_2; Δ is the momentum transfer to the nucleon; the longitudinal momentum flow corresponds to $\xi \mp \eta$ for the virtual photons, and $x \pm \eta$ for the partons.

DDVCS is the most general case of the deeply virtual Compton scattering (DVCS) in which the initial virtual photon transforms into a real photon in the final state. DVCS is the main focus of existing and developing experimental programs since factorization was shown to hold already at electron beam energies of 6 GeV [17]. Several different experimental observables have been investigated, exhibiting expected sensitivity features to specific nucleon GPDs: polarized an unpolarized cross section off the proton [17, 18, 19, 20, 21] and off the neutron [22], beam spin asymmeties off the proton [23, 24, 25], target spin asymmetries off longitudinally [26, 27, 28, 29] and transversally [30] polarized protons, and beam charge asymmetries [31, 32]. Physics understanding and detection techniques attached to DVCS experiments did reach very high

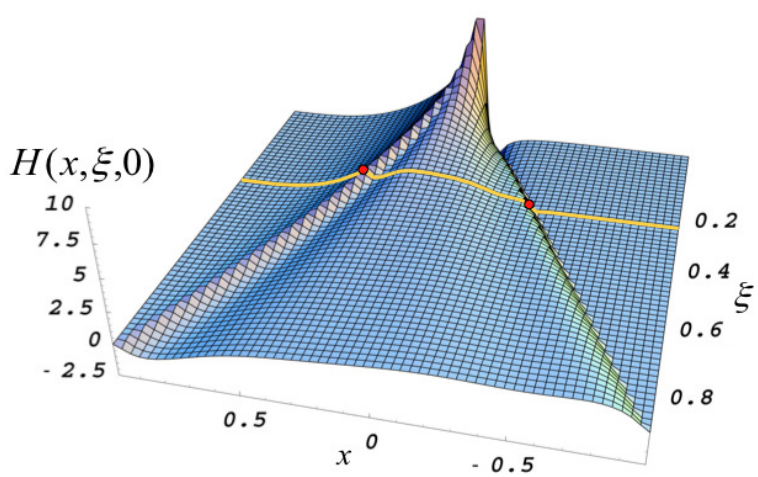

Figure 2: Graphical representation of the DVCS Compton form factor (CFF) showing a typical model for the GPD H at t=0; the red points indicates the GPD values involved in the CFF imaginary part, and the yellow line underlines the integral path of the CFF real part.

scientific maturity which enables today the ability to take full advantage of the next experimental program generation at JLab 12 GeV and COMPASS [33]. Future measurements of the DVCS process will allow for an unprecetended mapping of the nucleon GPDs via the separation of the Compton form factors (CFF), however limited to unambiguous interpretation only along specific correlation lines in the full GPDs kinematic phase-space. For instance, the CFF $\mathcal{H}$ associated with the GPD H and accessible in DVCS polarized cross section or beam spin asymmetry experiments can be written

$$\mathcal{H}(\xi,t) = \sum_q e_q^2 \left\{ \mathcal{P} \int_{-1}^{1} dx\, H^q(x,\xi,t) \left[\frac{1}{\xi - x} - \frac{1}{\xi + x} \right] + i\pi \left[H^q(\xi,\xi,t) - H^q(-\xi,\xi,t) \right] \right\} \qquad (1)$$

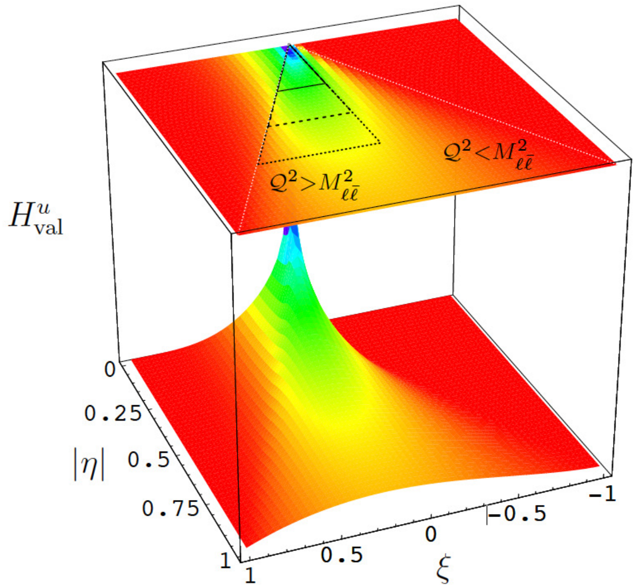

Figure 3: Example of coverage of the GPD surface for different electron beam energies and similar kinematic conditions [16]: 11 GeV (solid line), 25 GeV (dashed line), and 40 GeV (dotted line) in the GPD physics phase space $Q^2 > Q^{\text{‘}2}$.

where the sum runs over all parton flavors with elementary electrical charge e_q, and $\mathcal{P}$ indicates the Cauchy principal value of the integral. While the imaginary part of the CFF accesses the GDP values at $x = \pm\xi$, it is clear from Eq. 1 that the real part of the CFF is a more complex quantity involving the convolution of parton propagators and the GPD values out-of the diagonals $x = \pm\xi$ (Fig. 2), that is in a domain that cannot be resolved unambiguously with DVCS experiments. Because of the virtuality of the final state photon, DDVCS provides a way to circumvent the DVCS limitation [13, 14], allowing to vary independently x and ξ. Considering the same GPD H, the corresponding CFF for the DDVCS process writes

$$\mathcal{H}(\xi,\eta,t) = \sum_q e_q^2 \left\{ \mathcal{P} \int_{-1}^{1} dx \, H^q(x,\eta,t) \, \left[\frac{1}{\xi - x} - \frac{1}{\xi + x} \right] + i\pi \left[H^q(\xi,\eta,t) - H^q(-\xi,\eta,t) \right] \right\} \tag{2}$$

involving the additional scaling variable η representing here the GPD skewdness (Fig. 1). This variable obviously provides the necessary lever arm to investigate the GPD values out-of the diagonals (Fig. 3), that is resolving part of the phase space of interest for the CFF real parts of both DVCS and DDVCS. The kinematically allowed phase space for out-of diagonal exploration is an increasing function of the beam energy but still remains significant at 11 GeV (Fig. 3).

While being theoretically a very attractive process the major experimental difficulties are the reduced cross section induced by the lepton pair decay at the materialisation vertex of the final state photon, and the ambiguity bewteen the scattered and decay electrons when investigating the e^+e^- pair production. Additionally, eventual contamination from vector meson decay is putting constraints on the experimental phase space that further reduce the coverage efficiency of an experiment. These latter features did forbid any reliable GPD study from the low statistics data collected with CLAS in a tentative exploratory attempt. This letter-of-intent proposes to solve these issues by taking advantage of the luminosity capabilities of the SoLID spectrometer, and detecting the $\mu^+\mu^-$ di-muon pair from the virtual photon decay.

2.2 Kinematics

The kinematic parametrization of the DDVCS process, expressed in the reference frames of Fig. 4, can be noted

$$e(k) - e'(k') + p(p_1) \equiv \gamma^\star(q_1) + p(p_1) \to p'(p_2) + \gamma^\star(q_2) \to p'(p_2) + l^+(\mu^+) + l^-(\mu^-) \tag{3}$$

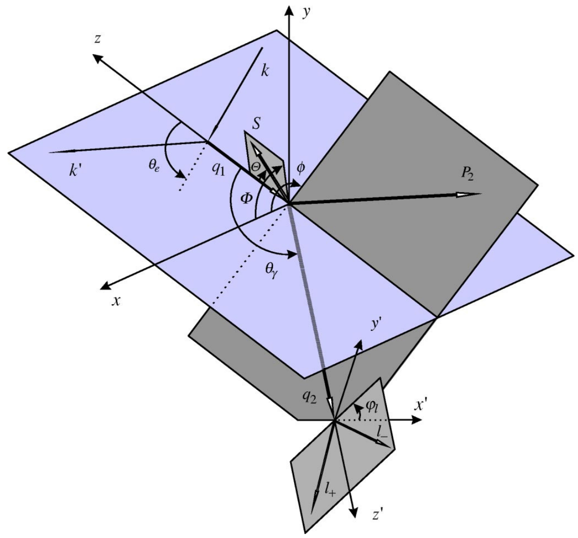

Figure 4: Reference frames for the DDVCS reaction.

where the photon virtualities write

$$Q^2 = -q_1^2\,, \qquad Q'^2 = q_2^2\,. \tag{4}$$

Defining the symmetrical variables p and q

$$q = \frac{1}{2}(q_1 + q_2)\,, \qquad p = p_1 + p_2\,, \tag{5}$$

and the four-momentum transfer to the nucleon $\Delta = p_1 - p_2 = q_2 - q_1$ with $t = \Delta^2$, the DDVCS scaling variables write

$$x_B = -\frac{1}{2}\,\frac{q_1 \cdot q_1}{p_1 \cdot q_1}\,, \qquad \xi = -\frac{q \cdot q}{p \cdot q}\,, \qquad \eta = \frac{\Delta \cdot q}{p \cdot q}\,. \tag{6}$$

Noting that

$$q^2 = -\frac{1}{2}\left(Q^2 - Q'^2 + \frac{\Delta^2}{2}\right) \tag{7}$$

one gets

$$\xi = \frac{Q^2 - Q'^2 + (\Delta^2/2)}{2(Q^2/x_B) - Q^2 - Q'^2 + \Delta^2}\,, \qquad \eta = -\frac{Q^2 + Q'^2}{2(Q^2/x_B) - Q^2 - Q'^2 + \Delta^2}\,, \tag{8}$$

which expresses GPDs variables of interest in terms of experimentally measured quantities. The different Q'^2-dependence in the numerators of ξ and η expresses the ability to access out-of diagonals phase space, however limited by experimental and physics constraints.

The available experimental DDVCS phase space for di-muon production at 11 GeV incident electron beam energy is represented on Fig. 5 in the (x_B, Q^2) plane: the inner space delimited by the full black lines corresponds to the kinematically allowed region; it is further restricted by the 1 GeV^2 lower Q^2-limit required at minima for the factorization of soft and hard scales, and the 4 GeV^2 lower W^2-limit insuring a deep inelastic process. Experimental constraints specific of the di-muon channel are expressed by the selection of the final virtual photon mass above 3 GeV^2 to minimize eventual contamination from vector mesons decay, leading to a minimum Q^2 (black dashed-line of Fig. 5). The SoLID spectrometer constraints is indicated by the blue lines corresponding to the 8°-25° angular coverage of the electron detector package. The combination of these different constraints yields the shaded area of Fig. 5. The additional red line separates the region $Q'^2 > Q^2$ (lower part) from the region $Q'^2 < Q^2$ (upper part), as a consequence of the minimum experimental Q'^2 requirement. The latter region is considered the domain of physics interest for applicability of the GPD formalism. Eq. 8 can be recast in

$$\xi = \frac{x_B}{2 - x_B}\,\frac{1 - (Q'^2/Q^2) + (\Delta^2/2Q^2)}{1 - [x_B(Q'^2 - \Delta^2)/(2 - x_B)/Q^2]}\,, \qquad \eta = -\xi\,\frac{1 + (Q'^2/Q^2)}{1 - (Q'^2/Q^2) + (\Delta^2/2Q^2)}\,, \tag{9}$$

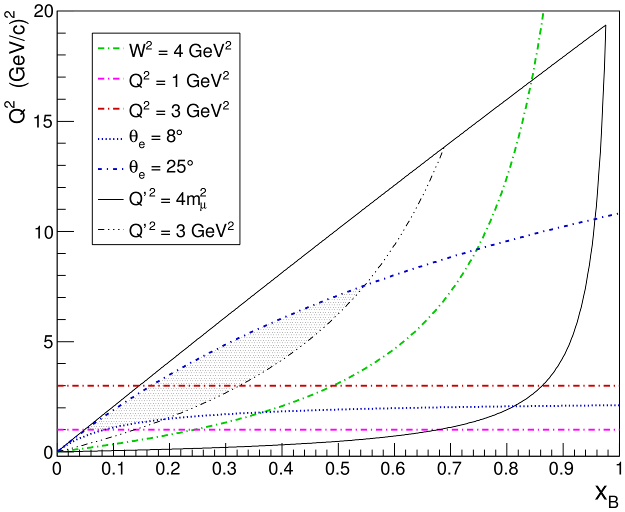

Figure 5: DDVCS experimental phase space for di-muon production at 11 GeV incident electron beam energy.

showing that in the forward limit the DVCS process accesses the region $\eta = -\xi$ ($\cong x_B/(2-x_B)$), as noted previously. The (ξ, x_B) and (η, ξ) longitudinal momentum fraction phase space at Δ^2_{min} is shown on Fig. 6 for the SoLID experimental phase space indicated by the hatched area of Fig. 5. In both panels, the region delimited by the black lines corresponds to the full hatched area of Fig. 5 and the red area underlined the region $Q'^2 < Q^2$. The blue area corresponds to the DVCS phase space that would be covered under the same detection conditions but the maximum Q^2 restricted in this case by the condition $W > 2$ GeV$/c^2$; one notices that the Δ^2-dependence is responsible from small deviations from the $\eta = -\xi$ line. In the most restricted case, the hyper-volume region corresponding to $x_B \in [0.17; 0.55]$, $Q^2 \in [3.0; 7.5]$, and $Q'^2 < Q^2$ would be explored, substanding the phase space $\xi \in [-0.10; 0.21]$ and $\eta \in [-0.78; -0.20]$. Depending on true background conditions, one may access moderately larger phase space possibly extending up to the same W-limit as DVCS. The region $Q'^2 > Q^2$ would also allow to reach higher Q'^2, however within a different physics regime.

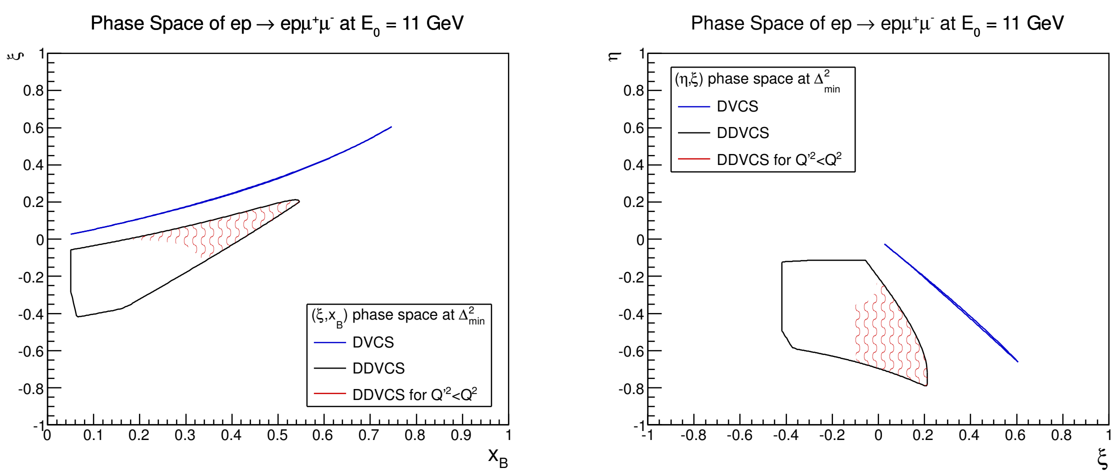

Figure 6: Longitudinal momentum fractions phase space for di-muon production at 11 GeV incident electron beam energy: (ξ, x_B) (left panel), and (η, ξ) (right panel).

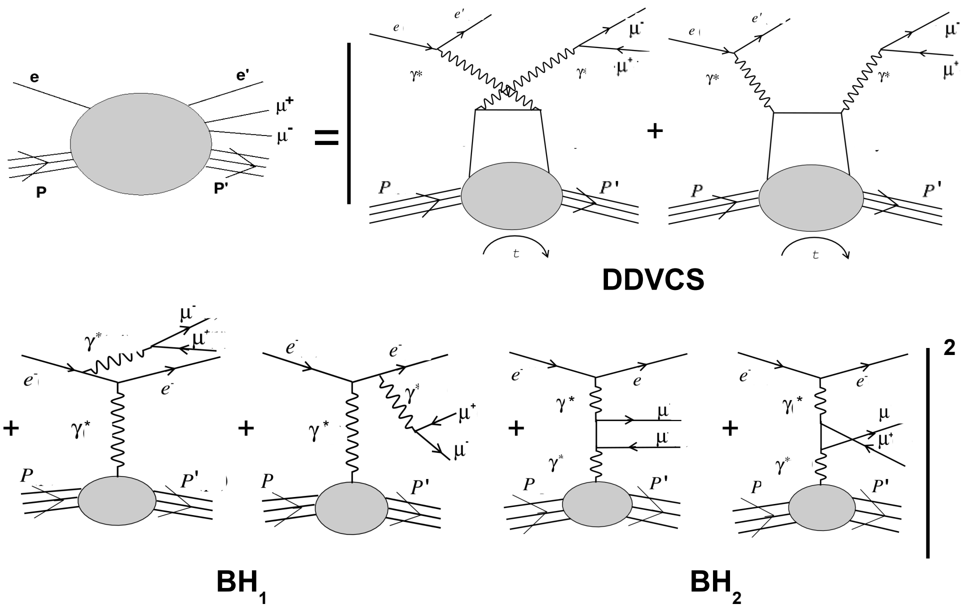

Figure 7: The different amplitudes contributing to the electroproduction of di-muons: the DDVCS, di-muon production from the initial and final leptons (BH_1), and the di-muon virtual production in the nuclear field (BH_2).

2.3 Cross section

As the electroproduction of photons, di-muon electroproduction proceeds through the coherent sum of two essential processes: the DDVCS and the Bethe-Heitler (BH) mechanisms (Fig. 7). The latter process corresponds traditionally to the radiation of a photon by the incoming or outgoing electron (BH_1) before or after interacting elastically with the nucleon. In the case of di-muon electroproduction, another Bethe-Heitler like process occurs involving the virtual production of di-muons in the nuclear field (BH_2). Having the same final state, the cross section for the electroproduction of di-muons is built from the coherent interference of these processes. Depending on the incident beam energy the ratio of the DDVCS to BH contributions would change in favor of the DDVCS amplitude as the beam energy increases. The differential cross section for the electroproduction of di-muon off the nucleon may be written [16]

$$\frac{d^7\sigma}{dx_B\, dy\, dt\, d\phi\, dQ'^2\, d\Omega_\mu} = \frac{1}{(2\pi)^3}\,\frac{\alpha^4}{16}\,\frac{x_B y}{Q^2\sqrt{1+\varepsilon^2}}\sqrt{1-\frac{4m_\mu^2}{Q'^2}}\,|\mathcal{T}|^2 \tag{10}$$

where the reaction amplitude can generically be expressed as

$$|\mathcal{T}|^2 = |\mathcal{T}_{VCS}|^2 + \mathcal{I}_1 + \mathcal{I}_2 + |\mathcal{T}_{BH_1}|^2 + |\mathcal{T}_{BH_2}|^2 + \mathcal{T}_{BH_{12}} \tag{11}$$

featuring the pure DDVCS amplitude $|\mathcal{T}_{VCS}|^2$, the interference amplitudes $\mathcal{I}_1$ and $\mathcal{I}_2$ between the DDVCS and Bethe-Heitler processes, and the pure BH amplitude built itself from the two elementary processes shown on Fig. 7. Following Ref. [16], the harmonic structure of the cross section writes

$$|\mathcal{T}_{VCS}|^2 = \frac{2\xi^2}{Q^4 y^2 \tilde{y}^2(\eta^2-\xi^2)} \quad \sum_{n=0}^{2} \quad \left[c_n^{VCS}(\varphi_\mu)\cos(n\phi) + s_n^{VCS}(\varphi_\mu)\sin(n\phi)\right] \tag{12}$$

$$\mathcal{I}_1 = \frac{2\xi(1-\eta)}{Q^2\Delta^2 y^3\tilde{y}^3(\eta^2-\xi^2)}\,\frac{\tilde{y}}{P_1 P_2} \quad \sum_{n=0}^{3} \quad \left[c_n^{1}(\varphi_\mu)\cos(n\phi) + s_n^{1}(\varphi_\mu)\sin(n\phi)\right] \tag{13}$$

$$\mathcal{I}_2 = \frac{2\xi(1-\eta)}{Q^2\Delta^2 y^3 \tilde{y}^3(\eta^2-\xi^2)} \, \frac{y}{P_3 P_4} \quad \sum_{n=0}^{3} \quad \left[c_n^2(\phi)\cos(n\varphi_\mu) + s_n^2(\phi)\sin(n\varphi_\mu)\right] \tag{14}$$

$$|\mathcal{T}_{BH_1}|^2 = -\frac{\xi(1-\eta)^2}{Q^2\Delta^2 y^4 \tilde{y}^4 \eta(\eta^2-\xi^2)} \left(\frac{\tilde{y}}{P_1 P_2}\right)^2 \quad \sum_{n=0}^{4} \quad \left[c_n^{11}(\varphi_\mu)\cos(n\phi) + s_n^{11}(\varphi_\mu)\sin(n\phi)\right] \tag{15}$$

$$|\mathcal{T}_{BH_2}|^2 = -\frac{\xi(1-\eta)^2}{Q^2\Delta^2 y^4 \tilde{y}^4 \eta(\eta^2-\xi^2)} \left(\frac{y}{P_3 P_4}\right)^2 \quad \sum_{n=0}^{4} \quad \left[c_n^{22}(\phi)\cos(n\varphi_\mu) + s_n^{22}(\phi)\sin(n\varphi_\mu)\right] \tag{16}$$

$$\mathcal{T}_{BH_{12}} = -\frac{\xi(1-\eta)^2}{Q^2\Delta^2 y^4 \tilde{y}^4 \eta(\eta^2-\xi^2)} \, \frac{y\tilde{y}}{P_1 P_2 P_3 P_4} \quad \sum_{n=0}^{3} \quad \left[c_n^{12}(\varphi_\mu)\cos(n\phi) + s_n^{12}(\varphi_\mu)\sin(n\phi)\right] \tag{17}$$

where the P_i's correspond to the propagators of the intermediate leptons of the BH processes

$$P_1 = -\frac{1}{2\eta}\frac{(k'+\Delta)^2}{p\cdot q} \quad P_2 = -\frac{1}{2\eta}\frac{(k-\Delta)^2}{p\cdot q} \quad P_3 = \frac{1}{2\eta}\frac{(\mu_+ +\Delta)^2}{p\cdot q} \quad P_4 = \frac{1}{2\eta}\frac{(\mu_- +\Delta)^2}{p\cdot q}\,. \tag{18}$$

The Fourier coefficients write

$$c_n^i(\alpha) = \quad \sum_{m=0}^{2} \quad \left[cc_{nm}^i \cos(m\alpha) + cs_{nm}^i \sin(m\alpha)\right] \tag{19}$$

$$s_n^i(\alpha) = \quad \sum_{m=0}^{2} \quad \left[sc_{nm}^i \cos(m\alpha) + ss_{nm}^i \sin(m\alpha)\right] \tag{20}$$

for $i \equiv (VCS, 1, 2, 11, 12, 22)$ and $\alpha \equiv (\varphi_\mu, \phi)$, correspondingly. Similarly to the single DVCS process, the $cc_{nm}^{VCS}, cs_{nm}^{VCS}, sc_{nm}^{VCS}, ss_{nm}^{VCS}$ coefficients are bi-linear combinations of Compton form factors, the coefficients for $i = 11, 12, 22$ are combinations of the nucleon electric and magnetic form factors, and the interference coefficients are linear combinations of the Compton form factors similar to the combinations measured in single DVCS. The full expression of the Fourier coefficients is lengthy detailed in Ref. [16]. It is worth noticing the symmetry properties of the BH propagators which obey

$$P_i(\phi) \quad = \quad P_i(2\pi - \phi) \tag{21}$$

$$P_j(\theta_\mu, \varphi_\mu) \quad = \quad P_j(\pi - \theta_\mu, \varphi_\mu + \pi) \tag{22}$$

for $i = \{1, 2, 3, 4\}$ and $j = \{3, 4\}$. As a consequence, the integration over $d\theta_\mu$ in a symmetric interval around θ_μ=$\pi/2$ for any definite moment in θ_μ reduces to a characteristic $\cos(k\varphi_\mu)$ Fourier expansion.

2.4 Beam spin asymmetry

Similarly to the DVCS reaction, the interference amplitude bewteen the BH and DDVCS processes is the observable of interest since it involves linear combinations of Compton form factors, which real an imaginary parts can be accessed in beam charge asymmetry and beam spin asymmetry experiments, respectively, and would ideally be measured by comparing polarized electron and polarized positron scatterings [34]. Considering the harmonic dependence of the cross section, it was shown [16] that the same basic information about GPDs can be obtained from the appropriate moments in ϕ or φ_μ, a feature of particular interest for experimental consistency. Taking advantage of the symmetry properties of the BH propagators to minimize the BH contribution, the first ϕ-moment and φ_μ-moment of the beam spin asymmetry can be written [16]

$$\begin{aligned}
\left\{ \begin{array}{c} A_{\rm LU}^{\sin\phi} \\ A_{\rm LU}^{\sin\varphi_\mu} \end{array} \right\} \quad &= \quad \frac{1}{\mathcal{N}} \int_{\pi/4}^{3\pi/4} d\theta_\mu \int_0^{2\pi} d\varphi_\mu \int_0^{2\pi} d\phi \left\{ \begin{array}{c} 2\sin\phi \\ 2\sin\varphi_\mu \end{array} \right\} \frac{d^7\overrightarrow{\sigma} - d^7\overleftarrow{\sigma}}{dx_B\,dy\,dt\,d\phi\,dQ'^2\,d\Omega_\mu} \\
&\propto \, \Im\mathrm{m}\left\{ F_1\mathcal{H} - \frac{t}{4M_N^2}F_2\mathcal{E} + \xi(F_1+F_2)\widetilde{\mathcal{H}} \right\}\,,
\end{aligned} \tag{23}$$

with the normalization factor given by

$$\mathcal{N} = \int_{\pi/4}^{3\pi/4} d\theta_\mu \int_0^{2\pi} d\varphi_\mu \int_0^{2\pi} d\phi \, \frac{d^7\overrightarrow{\sigma} + d^7\overleftarrow{\sigma}}{dx_B\,dy\,dt\,d\phi\,dQ'^2\,d\Omega_\mu}\,, \tag{24}$$

and where we omit for clarity the (ξ, η, t)-dependence of the CFF. In the case of a proton target the measurement gives access to the out-of diagonal GPD H, while the neutron observable is more sensitive to the E GPD.

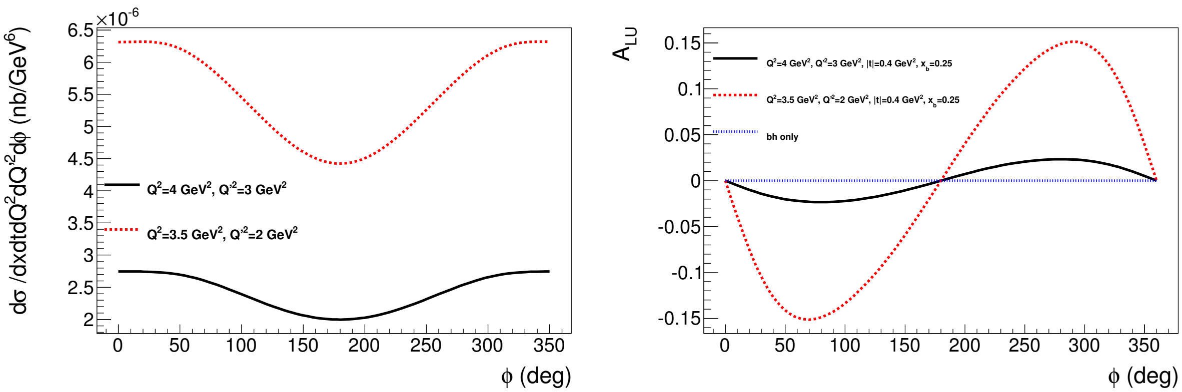

Figure 8: Out-of-plane angular dependence of the differential cross section (left) and the beam spin asymmetry (right) for the $^1\mathrm{H}(e, e'p\mu^+\mu^-)$ process at two selected kinematics at E=11 GeV.

Fig. 8 shows the differential cross section and the beam spin asymmetry A_{LU} from the VGG model [15] for the di-muon production process at two relevant kinematics for the determination of GPDs. These experimental observables have been obtained using the prescription of Eq. 23 for the integration over the angular phase space of the di-muon pair. Similarly to DVCS, the BH process alone on an umpolarized nucleon does not generate beam spin asymmetries. Sizeable asymmetries are predicted from the DDVCS and BH interference together with, as expected, a strong sensitivity of the cross section to kinematic conditions.

3 DDVCS benefits for the GPD program

Beyond the remarkable unification and universality power of the parametrization of the nuclear structure, GPDs provide new visual insight on the partonic structure of matter by allowing for a tomography of the nucleon [8, 10]. In the particular case of zero skewdness, GPDs acquire a well-defined probability interpretation in the infinite momentum frame, similarly to conventional parton distributions. Indeed, the impact parameter dependent parton distribution related to H^q can be written [36]

$$q(x, \mathbf{b}_\perp) = \frac{1}{(2\pi)^2} \int d^2\mathbf{\Delta}_\perp \, H^q(x, 0, -\mathbf{\Delta}_\perp^2) \, e^{-i\mathbf{b}_\perp \cdot \mathbf{\Delta}_\perp} \tag{25}$$

telling that $q(x, \mathbf{b}_\perp)$ is the Fourier transform of $H^q(x, 0, -\mathbf{\Delta}_\perp^2)$. Therefore, the knowledge of GPDs at zero skewdness allows to determine the probability to find a parton carrying the light-cone longitudinal momentum fraction x of the nucleon at a transverse distance $\mathbf{b}_\perp$ from the center of momentum. Since they are linked to form factors through the 0^{th}-order Mellin moment, GPDs can also be seen as a light-cone momentum decomposition of form factors. As today, access to zero skewdness GPDs for any momentum fraction x is only obtained from a model dependent interpretation of current DVCS data allowing for ξ-dependence extrapolation. Bringing uncorrelated information on the ξ-dependence of GPDs, DDVCS will ultimately allow for a model-independent interpretation of data providing a truely experimental determination of the parton transverse densities.

Additionally, the ξ-dependence of GPDs contains unique information about the distribution of nuclear forces. Polynomiality is a major property of GPDs which expresses that the n^{th} order Mellin moment of a GPD is a polynomial in ξ of maximal $(\mathrm{n}+1)^{\text{th}}$ order [6]

$$\int_{-1}^{1} dx \, x^n \sum_q H^q(x, \xi, t) = \sum_{i=0}^{n+1} \sum_q h_i^{q(n)}(t) \, \xi^n \, . \tag{26}$$

Following time reversal invariance, the polynomial expansion contains only even power of ξ [35], such that for instance

$$\int_{-1}^{1} dx \, x \sum_q H^q(x, \xi, t) = \sum_q h_0^{q(1)}(t) + \sum_q h_2^{q(1)}(t) \, \xi^2 \, . \tag{27}$$

Futhermore, because on the spin 1/2 of the nucleon, the coefficient of the highest power in ξ for the GPDs H^q and E^q are related [35], leading to

$$\int_{-1}^{1} dx\, x \sum_q E^q(x,\xi,t) = \sum_q e_0^{q(1)}(t) - \sum_q h_2^{q(1)}(t)\, \xi^2 \,, \tag{28}$$

consistently with the ξ-independence of the Ji sum rule [2]. Within the double distribution ansatz, the coefficient of the highest power in ξ is related to the so-called D-term which described GPDs out-of the diagonals $x = \pm\xi$ and therefore enters the real part of the corresponding DVCS CFF. The first Mellin moment of the H GPD can be recast

$$\int_{-1}^{1} dx\, x \sum_q H^q(x,\xi,t) = \sum_q M_2^q(t) + \frac{4}{5} \sum_q d_1^q(t)\, \xi^2 \tag{29}$$

where $d_1^q(t)$ is the first coefficient of the Gengenbauer expansion of the D-term [37]. In the forward limit, the first term of the right-hand side of Eq. 29 corresponds to the momentum fraction of the target carried by the quark q while the second term was shown to encode information about the spatial distribution of forces experienced by quarks and gluons inside hadrons [7]. Consequently, measuring the ξ-dependence of GPDs is providing an alternative access to the strong force distribution and would also provides a deeper investigation of the ξ-independence of the Ji sum rule.

4 The Solenoidal Large Intensity Device (SoLID)

4.1 Description

The SoLID spectrometer is based on the CLEO II solenoidal magnet [38] and is already supporting today a unique experimental program involving non-exhaustively

- Parity violation in deep inelastic scattering (PVDIS) [39];
- Semi-inclusive experiments (SIDIS) on polarized ^{3}He [40, 41] and NH_3 [42] targets;
- J/Ψ production at threshold on the proton [43].

The common grounds of these experiments are a full 2π azimuthal coverage and high luminosity requirements in the range 10^{37}-10^{39} cm$^{-2}\cdot$s^{-1}. Solenoidal geometry is the most suitable arrangement for high luminosity capabilities because of the trapping effect of the magnetic field on low energy background particles acting therefore as detector shielding. The detection capabilities developped for these experiments are essential for GPDs study, and particularly for a DDVCS experimental program. DDVCS involves the detection of muon pairs produced around the virtual photon defined by the scattered electron. In such a case, a full and symmetrical azimuthal angle coverage is a minimal requirement to allow for the determination of angular harmonics from the beam-spin asymmetry. The additionnal DDVCS constraint is the high luminosity needed to compensate small cross section about 1/100 of the DVCS one. SoLID is especially designed to achieve these goals and would be ideally suited for a DDVCS program.

The SoLID detection system is built around the solenoidal field of the CLEO II magnet having an uniform axial central field of 1.5 T, a large inner space with a clear bore diameter of 2.9 m, and a coil 3.1 m in diameter and 3.5 m in length which ensures a $\pm 0.2\%$ field uniformity. The magnet was built in the 1980s by the Oxford Company and installed for CLEO II in 1989 [38]. The main technology developped for the high luminosity purpose of the SoLID detector are Gas Electron Multiplier (GEM) systems arranged in three layers [44]. They allow tracking at high rates and are providing the momentum measurement capabilities of the spectrometer. The triple-GEM detectors permit large area detectors with high counting rate capabilities, exceeding 2.5 MHz/cm^2 [45], together with excellent spatial resolution $\sim$70 μm [46]. The main trigger is based on a shashlyk calorimeter constituting of 1800 preshower and shower hexagonal counters having good radiation hardness properties, moderate energy resolution about $10\%/\sqrt{E}$, and reasonable intrinsic pion rejection factor ($\sim$10). Pion contamination is further reduced by a Light Gas Čerenkov (LGC) detector placed before the calorimeter and constituting of 30 sectors, each read by 9 PMTs for a total number of 270 channels.

A cryogenic target is under developement for the PVDIS experiment, allowing for target placement inside the SoLID magnet. Operating at 19 K and 0.17 MPa, the target density is 0.0723 g·cm^3 allows to achieve the luminosity

$$\mathcal{L} = \frac{I}{e} L \mathcal{N} \frac{\rho}{A} = 0.32 \times 10^{39} \text{ cm}^2 \cdot \text{s}^{-1} \tag{30}$$

for a 15 cm long target. This length is quoted here as a secure reference length but may be increased, depending on the spectrometer characteristics and detector rate capabilities. In the case of SoLID at 80 μA beam current, a 40 cm long target at 18 K would allow to gain about a factor 3 on the luminosity reaching 0.88×10^{39}cm^2·s^{-1}. Higher luminosities can in principle be achieved with longer targets, though acceptance and boiling effects require special attention.

4.2 The J/Ψ setup

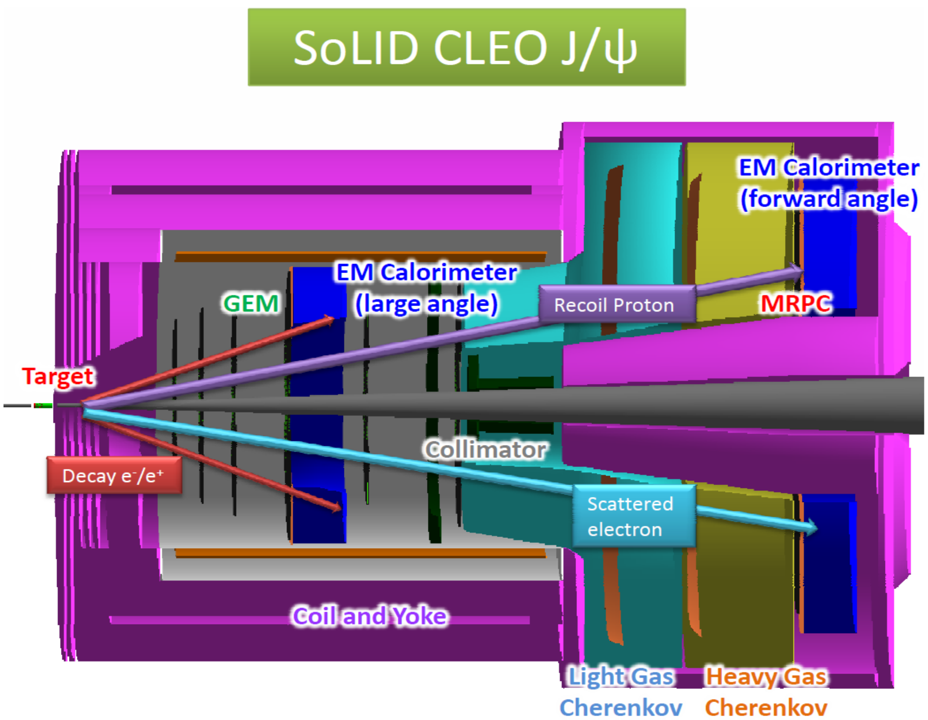

Figure 9: J/Ψ configuration of the SoLID spectrometer [41].

The J/Ψ experiment is using the SoLID spectrometer with a forward SIDIS configuration, the target located outside of the detector (Fig. 9). The experiment is designed to detect e^+e^- pairs from the J/Ψ decay and is planned for running at 3 μA on a 15 cm target long liquid hydrogen target, corresponding to the instantaneous luminosity 1.2×10^{37} cm^{-2}·s^{-1}. In addition to the Forward Angle Electromagnetic Calorimeter (FAEC) and the LGC, part of the FAEC at large angle will be reconfigured in a Large Angle Electromagnetic Calorimeter (LAEC) located inside the detector to cover angles from 16° to 24°. Expected single particle rates at this lumonisity are indicated on Tab. 1. The main trigger of that experiment is the 3-fold coincidence between the scattered electron and the two leptons from the J/Ψ decay. This triple coincidence yields a moderate trigger rate (a few kHz) allowing to run parasitically other trigger type. Additionally, the expected detector resolutions - 2% in momentum, 0.6 mr in polar angle and 5 mr in azimuthal angle - would be also suitable for a DDVCS experiment.

Process	Rate Forward Angle @ 11 GeV	Rate Large Angle @ 11 GeV
single e	0.34 MHz	0.04 MHz
high energy γ	7.5 MHz	0.40 MHz
single π^+	11 MHz	0.25 MHz
single π^-	7.0 MHz	0.18 MHz
single p	3.3 MHz	0.19 MHz

Table 1: Single particle rates at the J/Ψ experiment luminosity [41].

4.3 The DDVCS muon detector

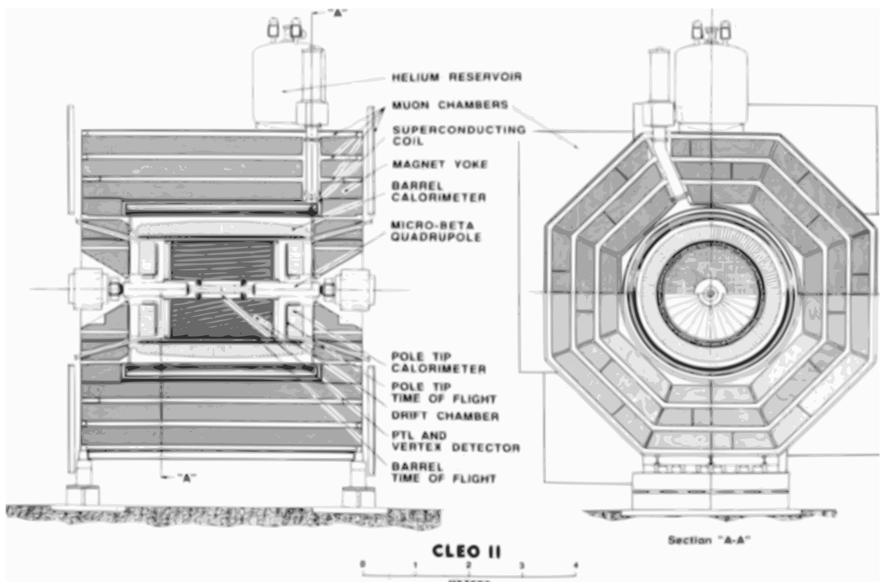

Figure 10: CLEO II setup with muon chambers installed inside the iron yoke.

As shown in Fig. 10, the CLEO II detector was equipped with muon chambers located inside the iron yoke of the magnet Each iron layer is 36 cm thick over a 5 m total length. The muon chambers are modular streamer technology (Fig. 11) based on an elementary module 8 cm wide and comprising 8 sensitive wires. Several modules are assembled together to constitute the 5.0×1.2 m^2 chambers. We are proposing to complement the SoLID detector package with CLEO II muon chambers and add muon detection capabilities over a large angular phase space. In the case of SoLID, the beam line height constraint allows using the first two layers of iron, leaving part of the iron material and the third layer chambers available. We are thus proposing to recover also the third muon detection layer and provide muon detection at forward angles based on the relocation of the third muon detection layer at the end-cap of SoLID. Such addition would not only establish the capability to achieve a di-muon DDVCS experimental program but would also contribute to statistics increase of the J/Ψ experiment, and would add permanent muon-detection capabilities to SoLID.

Since muons leave low energy in the calorimeter, a dedicated muon triggers has to be developped based on the detectors located after the calorimeter. Indeed since muons are heavy leptons they radiate much less than electrons and can get through large amount of materials. The signal for triggering will be provided by the discrimination of muon chambers signals that will be further fed into a JLab custom logic module. It is a 250 MHz pipeline module able to built coincidence every 4 ns at 1 ns resolution. The trigger will search for coincidence between several layers of trackers looking for zone of interest and clean tracks. The

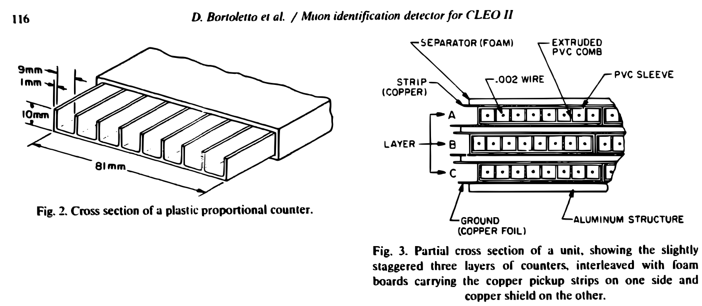

Figure 11: Mechanical configuration of CLEO II muon chambers.

muon trigger will look for the coincidence of two candidate muon tracks to reduce the effect of single pion background. The main trigger will be a coincidence between the standard calorimeter trigger and the muon detector. Additional lower level triggers would also be implemented for a precise understanding of the detectors acceptances and efficiencies. Scintillators or gaseous detectors may also be considred to complement or substitute muon chambers at forward angles.

5 Proposed parasitic experiment

The DDVCS experimental program at SoLID is proposed to develop according to two sucessive steps: a first parasitic run, followed by a dedicated run at a later time. The parasitic data taking would be parallel to the J/Ψ experiment run and would involve supplementing the J/Ψ setup with the original CLEO II muon chambers, implementing muon detection at forward angles, and developping a specific muon trigger along the lines previously discussed. This first step is expected to deliver a significant set of experimental data about di-muon production at different deep-inelastic regimes, and to bring data for GPD physics at $Q^2 > Q'^2$ in a limited phase space region. The dedicated run will take advantage of a strong luminosity increase and a specific detector configuration to realize the full physics potential accessible at 11 GeV for GPDs via DDVCS.

5.1 DDVCS acceptance

The acceptance of the muon supplemented J/Ψ setup (J/Ψ-μ setup herefater) under di-muon production conditions at 11 GeV was studied using the GEMC simulation package and an event generator based on the di-muon BH processes. As a reminder, the electron acceptance covers 8-14.5° for the forward angle calorimeter and 16-25° for the large angle calorimeter. This small angular detection hole is seen of the top left plot of Fig. 12 showing the scattered electron acceptance with a population distribution characteristics of the dominance of low Q^2 cross sections. Correspondingly, recoil protons are localiszed at large angles and small energy covering the t-acceptance about -t <2.0 GeV^2, especially relevant for GPD studies at JLab energies. Decay muons are most likely emitted at forward angles (Fig. 12 bottom panel); the apparent disconnection coverage at ∼20° originates from the muon-detector configuration organized in a forward sector at the SoLID end-cap and a larger angle region around the solenoid magnet.

The physics coverage in the (Q^2, x_B) phase space (Fig. 13) was studied using a VGG [15] based event generator [47] focussed on the kinematics region of interest. The black area overlayed on Fig. 13 takes into account the acceptance function of the J/Ψ-μ setup together with the physics cut $Q'^2 > 3$ GeV^2. The limitation of the high Q^2 coverage comes from the angular acceptance of the large angle calorimeter while the gap between the blackened areas corresponds to the gap between calorimeters.

5.2 Expected rates and results

The main DDVCS trigger will be the coincidence between an electron and a muon pair. The luminosity during the J/ψ experiment is planned to be 10^{37} cm^{-2}·s^{-1} and may be increased moderately depending on

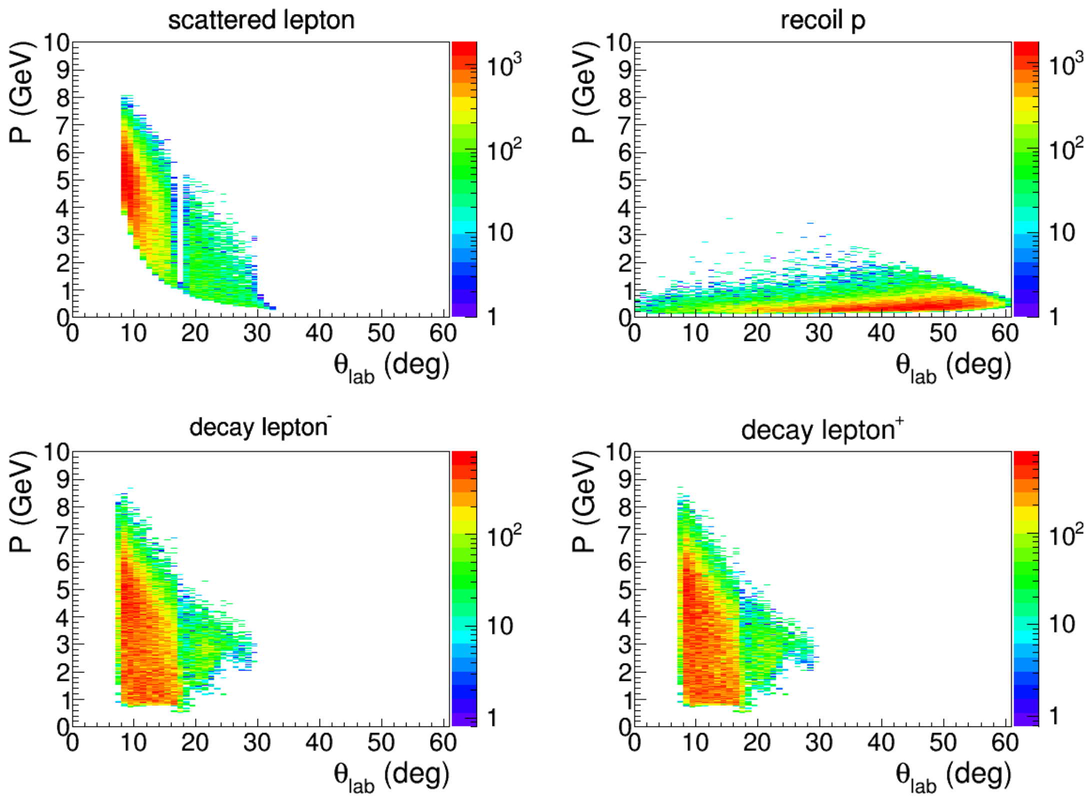

Figure 12: Electron (top left), proton (top right), and muon (bottom) acceptances supported by the J/Ψ-μ setup; angles are referenced in the SoLID laboratory frame.

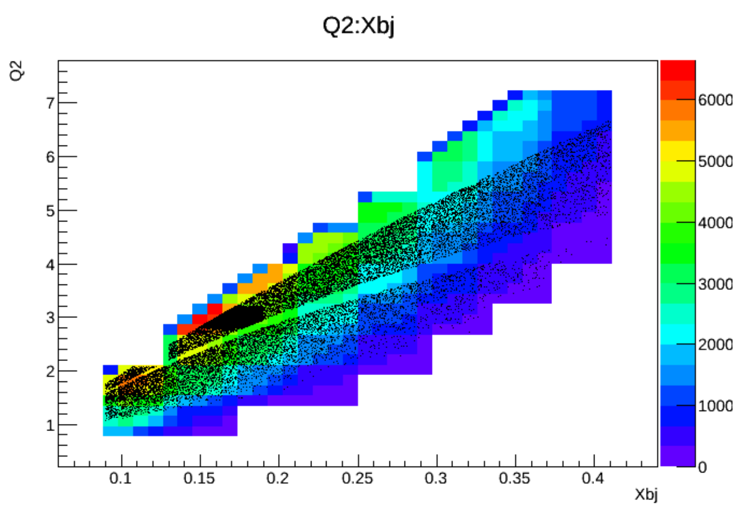

Figure 13: DDVCS physics acceptance of the J/Ψ-μ setup represented by the blackened area overlayed on a restricted region of the kinematics phase space. The black point density was kept low to allow for a better reading.

the detector background conditions. The J/Ψ-μ setup will double the statistics of the J/Ψ experiment by allowing for the detection of the di-muon decay channels simultaneously to e^+e^- pairs.

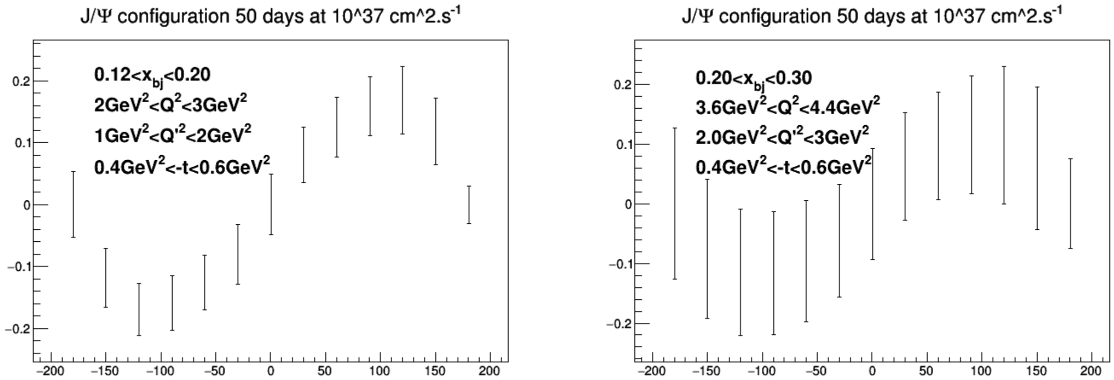

Figure 14: Expected beam spin asymmetries and statistical errors at two selected DDVCS kinematics for the J/Ψ-μ setup.

The expected DDVCS counting rates are high in the region x_B=0.12-0.20 at moderate Q^2=2.5 GeV^2, Q'^2=1.5 GeV^2, and 0.4 GeV^2 $<|t|<$0.6 GeV^2 for which we may expect a reasonnable ϕ-binning. Fig. 14-left is showing the expected asymmetry and statistics for that selected kinematics demonstrating the actual feasability of the experiment. In order to minimize contamination from meson decay, a minimum value of the final virtual photon mass is required i.e. $Q'^2>$3 GeV^2 inspired from photoproduction experiments. However, the final experimental value of this ad-hoc cut may be lower depending on the true cross section for the electroproduction of meson at DDVCS kinematics. There exists some indications [13] supporting reduced cross sections that would allow to relax this cut and access high counting rate regions. The first parasitic step proposed here would answer such questions while simultaneously providing a set of experimental data for di-muon electroproduction at different physics regimes. However, in the high Q^2 and x_B region where DDVCS asymmetries are predicted to be small (Fig. 14-right), statistics will most likely be not large enough for a significant impact. Higher luminosities are needed to investigate this domain.

6 Proposed dedicated experiment

6.1 Detector configuration change

Since the J/Ψ experiment is focusing on cross-section tracking, optimization of the detector efficiencies is an important matter and hence the luminosity is constrained by the beam current limited at 3 μA. However, limitation from the parasitic J/Ψ measurement can be overcome using a dedicated setup. We are proposing in a second step to optimize the detector configuration for DDVCS measurements (Fig. 15) at larger Q^2 and x_B using the PVDIS target and complementing the detection system at large angles.

The PVDIS target allows to move the interaction point inside the magnet at 150 cm from the calorimeter instead of the 350 cm for the J/Ψ. This has several advantages :

- low energy background is trapped earlier by the magnetic field reducing the probability of interaction with materials;
- the angular acceptance to larger angle is enhanced for the large angle electrons, the muon pairs and the protons.
- the target length can be increased from 15 to 45 cm since large angular coverage is available.

Seeking for very high luminosity to access this phase space region, electrons would be only detected in the large angle calorimeter. The large angle calorimeter initially covering 16°-25° would cover 33°-54°, and

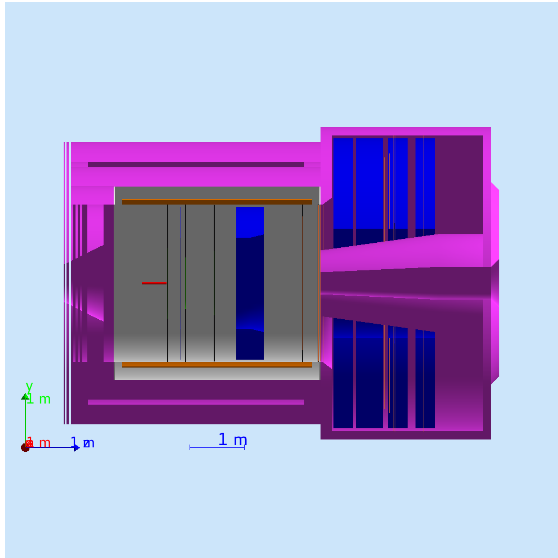

Figure 15: Schematic of the dedicated DDVCS detector arrangement: the target is inside the magnet and an iron plate is placed as close as possible to the magnet to shield the calorimeter low energy photons; the calorimeter is placed behind the iron plate; two additional iron plates interleaved with muon chambers are placed behind the calorimeter.

further blocks would be added to reach small angles down to 24°. A 36 cm iron plate would be placed in front of the calorimeter to reduce electromagnetic background and radiation damage, and the muon detector would be placed right after it. The calorimeter resolution would be consequently degraded but the full resolution on muon momentum would still be achieved because relying on the GEMs system in front of the calorimeter. The increase of the target length together with a moderate increase of the beam current at 10 μA will allow to reach a luminosity of $10^{38}\text{cm}^{-2}\cdot\text{s}^{-1}$.

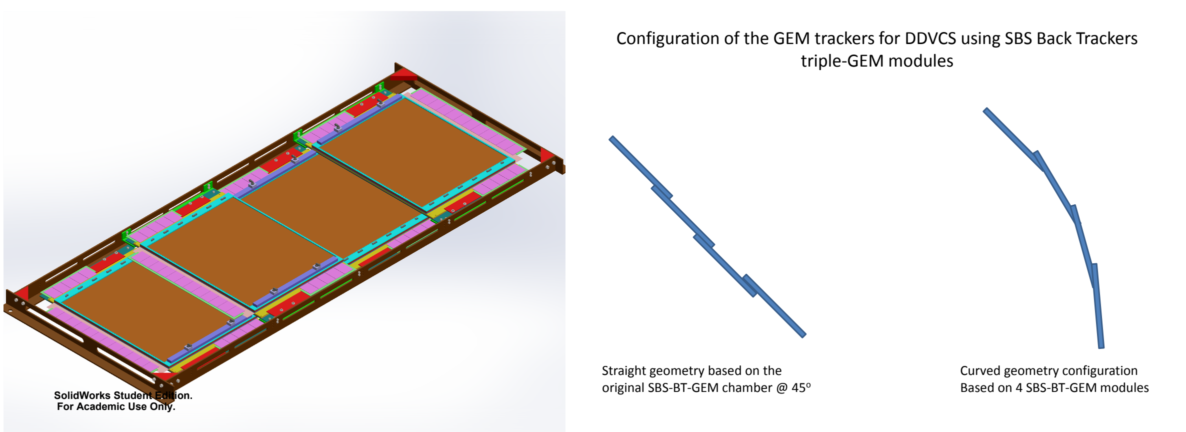

Figure 16: SBS back-tracker GEM chamber (left), and possible modular arrangement for DDVCS configuration.

The SoLID detector is designed as a forward solenoidal spectrometer with chambers being large vertical discs, not configured for the detection of large angle particles. We are proposing to supplement the GEM planes with additionnal trackers based on the SuperBigBite chamber design. In addition, the SuperBigBite spectrometer (SBS) back-tracker GEM (SBS-BT-GEM) [44], used for recoil proton polarimetry in the SBS, will be used for the determination of the momentum of large angle muons and protons. They consists of 10 layers of 200×60 cm^2 triple GEM chambers with each chamber assembled from a vertical stack of four SBS-BT-GEM modules (Fig. 16). The 40 SBS-BT-GEM modules with an active area of 50×60 cm^2 are being built at UVa. The SBS-BT-GEM module is based on the proven triple-GEM design [45] developped for the COMPASS experiment at CERN [45]. The large chambers in the original configuration for SBS will be positionned at 45° to increase the acceptance and improve resolution or alternatively in a curved configuration with minor arrangement of the modules as shown on Fig. 16. A conceptual schematic of the dedicated DDVCS detector configuration is shown on Fig. 15.

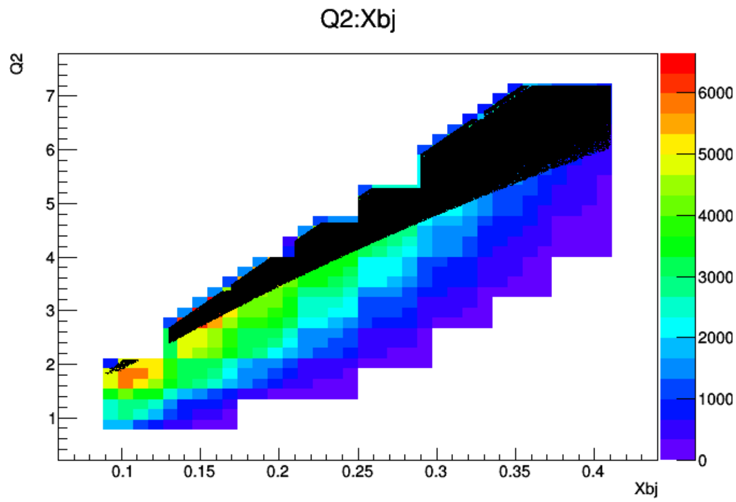

Figure 17: (x_B, Q^2) physics acceptance of the DDVCS dedicated setup represented by the blackened area overlayed on a restricted region of the kinematics phase space.

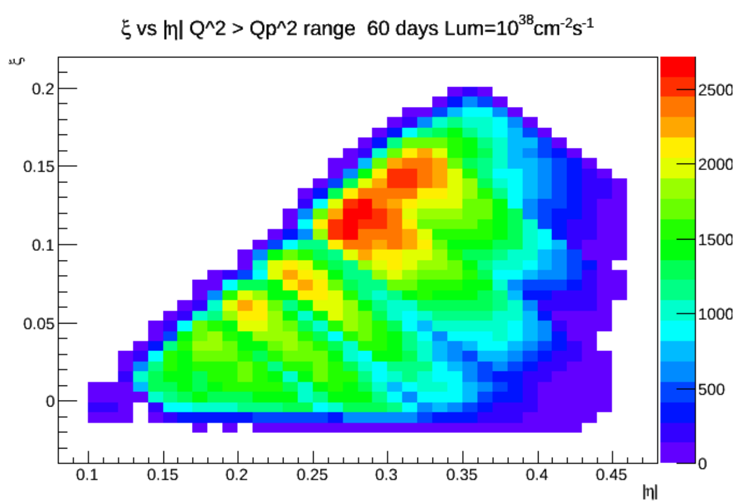

Figure 18: (ξ, η) physics acceptance of the DDVCS dedicated setup.

The scientific benefits of a dedicated experiment is indicated on Fig. 17 showing the physics phase space coverage in the (x_B, Q^2) plane. Similarly to Fig. 13, the blackened area indicates the detector acceptance coverage. The corresponding (ξ, η) phase space is shown on Fig. 18 supporting further the relevance of such a dedicated experiment.

The expected experimental asymmetries and statistics are reported on Fig. 19 for two selected kinematics. At high Q^2 and x_B, the combination of low cross sections are small asymmetries makes significant measurements more difficult to achieve. A factor 10 increase in the luminosity together with a longer running time (60 up to 100 days) would allow to accomplish a significant (ξ, η) scan. The lowest Q^2 statistics would be large enough to bin in several variables and extract data with intricated angular distribution. Even higher luminosities up to 6×10^{38} cm^{-2}·s^{-1} would permit multi-dimensionnal binning in the full accessible phase space, similarly to DVCS experiment. The ability to operate in such high luminoisty environnement is still to evaluate, particularly with respect to pion rejection capabilities.

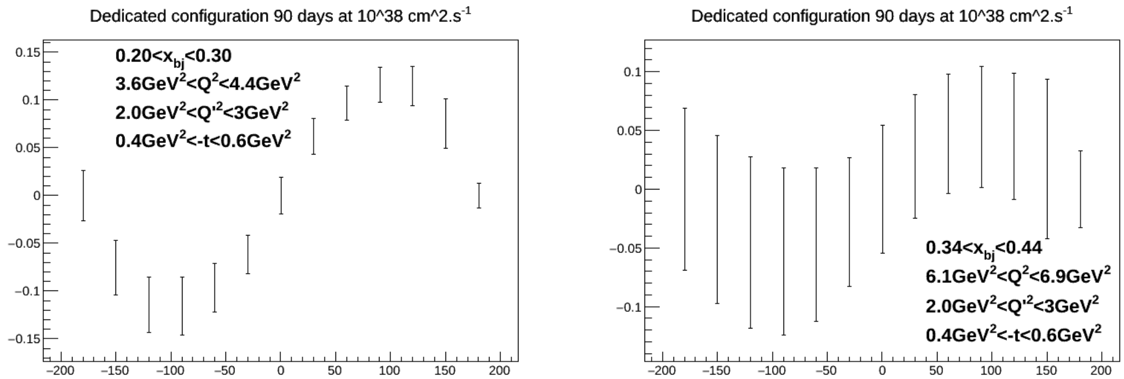

Figure 19: Expected beam spin asymmetries and statistical errors at two selected DDVCS kinematics for the DDVCS dedicated setup.

6.2 Directions of research for improved measurements

As for any large acceptance device, the luminosity is limited by rate capabilities and radiation hardness of the detectors. On-going R&D about high radiation hardness calorimeter is being developped for current experiments such as the SuperBigbite experiment, using lead-glass with constant curing at high temperature. Liquid scintillator based calorimeters or cryogenics sampling calorimeters are also being considered in order to provide fast response and high radiation hardness. Another domain being developped is superconducting photodetector and tracker. This has the potential to replace photomultipliers for calorimeter and gas Čerenkov counters and supplement the GEM trackers. Shorter pulse width from 10 ns down to 10 ps for the fastest superconductors would provide up to a factor 10 improvement in the rate capability. Thin copper GEM are being developped as well as Micromegas detector to reduce the amount of material and hence the photon conversion in the chamber, allowing for luminosity increase. Both GEM and Micromegas can already handle rates up to , the main issue being the optimization of the segmentation for occupance and cost. The trigger could also be improved by addition of a hadron blind gas Čerenkov detector which could fit the magnet. Finally pad tracker planes could be added to the tracker and to the muon detectors in order to reduce ambiguities. The goal of these developements is to reach the full luminosity available in Hall A ($\sim6\times10^{38}$ cm^{-2}·s^{-1}) which would allow a very fine binning in ξ and η.

7 Conclusion

We are proposing to reuse the CLEO II muon detector for the SoLID spectrometer to achieve a DDVCS experimental program. It would allow to complement the J/Ψ experiment by doubling the statistics in measuring di-muon decay channels, and would provide measurements of DDVCS in di-muon production. A first step, parasitic to the J/Ψ experiment, would open the investigation of this process and would guide a second dedicated step focusing on larger Q^2 and x_B. A dedicated setup is foreseen to sustain luminosities up to 6×10^{38} cm^{-2}·s^{-1}, providing a minimum factor 10 improvement as compared to the first step luminosity.

Those measurements would provide the necessary lever-arm to investigate GPDs out-of the diagonal regions, opening access to a fully experimental determination of parton transverse densities.

References

[1] D. Müller, D. Robaschick, B. Geyer, F.M. Dittes, J. Hořejši, Fortschr. Phys. **42**, 101 (1994).

[2] X. Ji, Phys. Rev. Lett. **78**, 610 (1997).

[3] A.V. Radyushkin, Phys. Rev. **D 56**, 5524 (1997).

[4] M. Diehl, Phys. Rep. **388**, 41 (2003).

[5] A. V. Belitsky, A. V. Radyushkin, Phys. Rept. **418**, 1 (2005).

[6] X. -D. Ji, Phys. Rev. D **55**, 7114 (1997).

[7] M. Polyakov, Phys. Lett. B **555**, 57 (2003).

[8] M. Burkardt, Phys. Rev. D **62**, 071503(R) (2000).

[9] J.P. Ralston, B. Pire, Phys. Rev. D **66**, 111501(R) (2002).

[10] M. Diehl, Eur. Phys. Jour. C **25**, 223 (2002).

[11] A.V. Belitsky, D. Müller, Nucl. Phys. A **711** (2002) 118c.

[12] A.V. Belitsky, D. Müller, A. Kirchner, Nucl. Phys. B **629**, 323 (2002).

[13] M. Guidal, M. Vanderhaeghen, Phys. Rev. Lett. **90**, 012001 (2003).

[14] A. V. Belitsky, D. Müller, Phys. Rev. Lett. **90**, 022001 (2003).

[15] M. Vanderhaeghen, P.A.M. Guichon, M. Guidal, Phys. Rev. D **60**, 094017 (1999).

[16] A. V. Belitsky, D. Müller, Phys. Rev. D **68**, 116005 (2003).

[17] (Hall A DVCS Collaboration) C. Muñoz Camacho *et al.*, Phys. Rev. Lett. **97**, 262002 (2006).

[18] (H1 Collaboration) C. Adloff *et al.*, Phys. Lett. B **517**, 47 (2001).

[19] (ZEUS Collaboration) S. Chekanov *et al.*, Phys. Lett. B **573**, 46 (2003).

[20] (CLAS Collaboration) H.S. Jo *et al.*, arXiv:hep-ex **1504.02009**, (2015).

[21] (Hall A DVCS Collaboration) M. Defurne *et al.*, arXiv:nucl-ex **1504.05453**, (2015).

[22] (Hall A DVCS Collaboration) M. Mazouz *et al.*, Phys. Rev. Lett. **99**, 242501 (2007).

[23] (HERMES Collaboration) A. Airapetian *et al.*, Phys. Rev. Lett. **87**, 182001 (2001).

[24] (CLAS Collaboration) S. Stepanyan *et al.*, Phys. Rev. Lett. **87**, 182002 (2001).

[25] (CLAS Collaboration) F.X. Girod *et al.*, Phys. Rev. Lett. **100**, 162002 (2008).

[26] (CLAS Collaboration) S. Chen *et al.*, Phys. Rev. Lett. **97**, 072002 (2006).

[27] (HERMES Collaboration) A. Airapetian *et al.*, JHEP **06**, 019 (2010).

[28] (CLAS Collaboration) E. Seder *et al.*, Phys. Rev. Lett. **114**, 032001 (2015).

[29] (CLAS Collaboration) S. Pisano *et al.*, Phys. Rev. D **91**, 052014 (2015).

[30] (HERMES Collaboration) A. Airapetian *et al.*, Phys. Lett. B **704**, 15 (2011).

[31] (HERMES Collaboration) A. Airapetian *et al.*, Phys. Rev. D **75**, 011103 (2007).

[32] (HERMES Collaboration) A. Airapetian *et al.*, JHEP **06**, 066 (2008).

[33] M. Boer, Doctorat Thesis, Université Paris Sud, IPNO **T-14-05**, (2014).

[34] E. Voutier, *Nuclear Theory*, Edts. A. Georgieva and N. Minkov, Heron Press, **33**, 142 (2014).

[35] P. Hoodbhoy, X. Ji, Phys. Rev. D **58**, 054006 (1998).

[36] M. Burkardt, Int. J. Mod. Phys. A **18**, 173 (2003).

[37] K. Goeke, M.V. Polyakov, M. Vanderhaeghen, Prog. Part. Nucl. Phys. **47**, 401 (2001).

[38] Y. Kubota *et al.*, Nucl. Inst. Meth. A **320**, 66 (1992).

[39] P. Souder, JLab Proposal **E12-10-007** (2010).

[40] J.P. Chen, H. Gao, X. Jiang, J.C. Peng, X. Qian, JLab Proposal **E12-10-006** (2010).

[41] J.P. Chen, Y. Qiang, W. Yan, JLab Proposal **E12-11-007** (2011).

[42] K. Allada, J.P. Chen, H. Gao, Z.E. Meziani, JLab Proposal **E12-11-108** (2011).

[43] K. Hafidi, X. Qian, Z.E. Meziani, N. Sparveris, Z. Zhao, JLab Proposal **E12-12-006** (2012).

[44] K. Gnanvo *et al.*, Nucl. Inst. Meth. A **782**, 77 (2015).

[45] C. Altunba *et al.*, Nucl. Inst. Meth. A **490**, 177 (2002).

[46] B. Ketzer *et al.*, Nucl. Inst. Meth. A **535**, 314 (2004).

[47] M. Boer, M. Guidal, *Private Communication*, (2015).